The Astrophysical Journal Letters, 890:L22 (8pp), 2020 February 20 https://doi.org/10.3847/2041-8213/ab72a5

$^{13}CH_3OH$ Masers Associated With a Transient Phenomenon in a High-mass Young Stellar Object

Xi Chen[1,2], Andrej M. Sobolev[3], Shari L. Breen[4], Zhi-Qiang Shen[2], Simon P. Ellingsen[5], Gordon C. MacLeod[6,7], Bin Li[2], Maxim A. Voronkov[8], Jane F. Kaczmarek[8,9], Jiangshui Zhang[1], Zhi-Yuan Ren[10], Jin Wang[1], Hendrik Linz[11], Todd R. Hunter[12], Crystal Brogan[12], Koichiro Sugiyama[13], Ross A. Burns[13,14], Karl Menten[15], Alberto Sanna[15], Bringfried Stecklum[16], Tomoya Hirota[13,17], Kee-Tae Kim[14], James Chibueze[18,19], and SP van den Heever[6]

[1] Center for Astrophysics, Guangzhou University, Guangzhou 510006, People's Republic of China; chenxi@gzhu.edu.cn
[2] Shanghai Astronomical Observatory, Chinese Academy of Sciences, 80 Nandan Road, Shanghai, 200030, People's Republic of China
[3] Ural Federal University, 19 Mira Street, 620002 Ekaterinburg, Russia
[4] Sydney Institute for Astronomy (SIfA), School of Physics, University of Sydney, NSW 2006, Australia
[5] School of Natural Sciences, University of Tasmania, Private Bag 37, Hobart, Tasmania 7001, Australia
[6] Hartebeesthoek Radio Astronomy Observatory, P.O. Box 443, Krugersdorp 1741, South Africa
[7] The University of Western Ontario, 1151 Richmond Street. London ON N6A 3K7, Canada
[8] CSIRO Astronomy and Space Science, Australia Telescope National Facility, P.O. Box 76. Epping, NSW 1710, Australia
[9] CSIRO Astronomy and Space Science, CSIRO Parkes Observatory, P.O. Box 276, Parkes NSW 2870, Australia
[10] National Astronomical Observatories, Chinese Academy of Science, Datun Road A20, Beijing, People's Republic of China
[11] Max Planck Institute for Astronomy, Königstuhl 17, D-69117 Heidelberg, Germany
[12] The National Radio Astronomy Observatory, 520 Edgemont Road, Charlottesville, VA 22903, USA
[13] Mizusawa VLBI Observatory, National Astronomical Observatory of Japan (NAOJ), 2-21-1 Osawa, Mitaka, Tokyo 181-8588, Japan
[14] Korea Astronomy and Space Science Institute, 776 Daedeokdae-ro, Yuseong-gu, Daejeon, 34055, Republic of Korea
[15] Max-Planck-Institut für Radioastronomie, Auf dem Hügel 69, D-53121 Bonn, Germany
[16] Thüringer Landessternwarte, Sternwarte 5, D-07778 Tautenburg, Germany
[17] Department of Astronomical Sciences, SOKENDAI (The Graduate University for Advanced Studies), Osawa 2-21-1, Mitaka-shi, Tokyo 181-8588, Japan
[18] Space Research Unit, Physics Department, North West University, Potchefstroom 2520, South Africa
[19] Department of Physics and Astronomy, Faculty of Physical Sciences, University of Nigeria, Carver Building, 1 University Road, Nsukka, Nigeria
Received 2020 January 13; revised 2020 January 30; accepted 2020 February 1; published 2020 February 20

Abstract

We report the first detection of isotopic methanol ($^{13}CH_3OH$) maser emission in interstellar space. The emission was detected toward the high-mass young stellar object G358.93-0.03 during monitoring of a flare in the 6.7 GHz methanol (CH_3OH) maser emission in this source. We find that the spectral and spatial distribution of the $^{13}CH_3OH$ masers differs from the CH_3OH masers imaged at the same epoch, contrary to expectations from similarity of their pumping. This conclusively demonstrates that isotopic methanol masers are bright under different physical conditions and suggests that they can provide additional, complementary information to the CH_3OH masers from the same source. We detect a rapid decay of the $^{13}CH_3OH$ maser lines suggesting that they are transient phenomena (masing for only a few months), likely associated with rapid changes in radiation field due to an accretion burst induced by massive disk fragmentation. Changes in the line flux density are faster than required to achieve equilibrium in the energy level populations, indicating that the pumping of these masers is likely variable.

Unified Astronomy Thesaurus concepts: Interstellar masers (846); Interstellar molecules (849); Stellar accretion disks (1579); Star formation (1569); Astrophysical masers (103)

Supporting material: machine-readable table

1. Introduction

Maser emission from transitions of the main methanol species $^{12}CH_3OH$ (hereafter CH_3OH) are unique tracers of the physical parameters (Cragg et al. 2005) and kinematics (Sanna et al. 2015, 2017) in dense gas regions within ~1000 au around high-mass young stellar objects (HMYSOs). CH_3OH maser emission has been detected from more than 40 different rotational transitions (Müller et al. 2004). The intense emission detected from some of the transitions, such as the 6.668 GHz (5_1–6_0 A^+) transition, provides us with an important probe of the formation and evolution of the most massive stars in the Milky Way (Ellingsen et al. 2007). Methanol maser transitions are empirically divided into two classes based on their relevant pumping mechanism (Menten 1991). Class I masers are pumped through collisional processes (Leurini et al. 2016) in regions where molecular gas is mildly shocked, such as protostellar outflows and expanding H II regions (Chen et al. 2013; Voronkov et al. 2014); Class II masers are exclusively observed near HMYSOs (Minier et al. 2003; Xu et al. 2008), and are pumped by far-infrared (FIR) radiation (Cragg et al. 2005).

The common detection of strong CH_3OH emission in interstellar environments suggests that in some circumstances it may also be possible to detect maser emission from isotopic methanol species. Theoretical calculations have suggested that the 5_1–6_0 A^+ and 2_0–3_{-1} E transitions of $^{13}CH_3OH$ (rest frequencies of approximately 14.300350 and 14.782270 GHz, respectively; Xu et al. 2014) are the most promising candidates for isotopic Class II methanol masers (Johns et al. 1998). These two transitions are the isotopic analogs of the strongest and most common Class II methanol maser transitions of CH_3OH (rest frequencies of 6.668 and 12.178 GHz, respectively). The previous searches for emission from the $^{13}CH_3OH$ transitions did not detect any masers in either (Kuiper et al. 1989; Menten & Batrla 1989). However, the 2_0–3_{-1} E (14.782 GHz) transition was detected in absorption toward three sources, Sgr A, SgrB2, and W33 (Kuiper et al. 1989).

In this Letter, we report the first detections of isotopic methanol ($^{13}CH_3OH$) masers. The detections were made toward the Galactic high-mass star-forming region G358.93-0.03. The 6.668 GHz Class II methanol maser toward this source has recently been reported to be undergoing a flaring event by the Maser Monitoring Organization (M2O).[20] The flare commenced around 2019 January 14 (Sugiyama et al. 2019). A number of new methanol transitions (about 20 new lines) have been found during its 6.668 GHz methanol flaring event by M2O members (Breen et al. 2019; Brogan et al. 2019; MacLeod et al. 2019). These detections include the first methanol masers from torsionally excited ($v_t = 1$ and 2) transitions (Breen et al. 2019; Brogan et al. 2019).

2. Observation and Data Reduction

2.1. Shanghai 65 m Tianma Radio Telescope (TMRT) Observations

The first observation of the 5_1–6_0 A^+ (14.300 GHz) and 2_0–3_{-1} E (14.782 GHz) $^{13}CH_3OH$ transitions toward G 358.93-0.03 were undertaken with the Shanghai 65 m TMRT on 2019 March 14. Clear detections of both transitions were made, but due to some instabilities in the backend system during these observations, we have not included the spectra in this Letter. In order to investigate the variability of the maser emission, monitoring observations of the two transitions were performed using the TMRT during 2019 April 2–15. For these observations, the cryogenically cooled Ku-band receiver and digital backend system were used. Two 23.4 MHz spectral windows, each with 32,768 channels, were used to observe the two transitions. This yielded a channel spacing of 0.715 KHz, corresponding to a velocity resolution of $\sim$0.015 km s^{-1}. The system temperature ranged between 60–70 K during the observations. The beam size was $\sim 1\farcm5$. Observations were targeted toward the reported 6.668 GHz methanol maser G 358.931−0.030 (J2000 position: $17^h43^m10\fs02$, $-29°51'45\farcs8$). The 6.668 GHz methanol masers have subsequently been found to be offset $\sim 1''$ from this position, but not to an extent that makes any significant difference to the sensitivity of the TMRT observations. Using the TMRT's active surface correction system, the achieved aperture efficiency of the telescope was $\sim$55%, corresponding to a sensitivity of 1.51 Jy K^{-1}. The uncertainty in the absolute flux density is less than 5%.

The observations were performed as a series of eight repetitions each with a 2 minute ON/OFF cycle. The total on-source time was 16 minutes for each observation. The typical rms noise of the observations was $\sim$0.1 Jy per spectral channel.

2.2. NSF's Karl G. Jansky Very Large Array (VLA) Observations

VLA B-array observations of $^{13}CH_3OH$ in the 5_1–6_0 A^+ (14.300 GHz) and 2_0–3_{-1} E (14.782 GHz) transitions, and CH_3OH in the 2_0–3_{-1} E (12.178 GHz) and 16_5–17_4 E (12.229 GHz) transitions were made on 2019 March 24. For each transition, a 4 MHz band with 1024 channels (corresponding to a velocity coverage of $\sim$85 km s^{-1} and channel spacing of 0.09 km s^{-1}) was used. Frequent observations of the quasar J1744−3116 (J2000 position: $17^h44^m23\fs5783$, $-31°16'36\farcs293$) were used to calibrate the time-dependent antenna gains. It should be noticed that this calibrator position was adopted with the value specified in the VLBA calibrator catalog, rather than that in the VLA online calibrator catalog. 3C286 was used to calibrate the bandpass response and flux density. The tracking center was the position of the 6.668 GHz methanol maser (same as the TMRT observations). The standard VLA Calibration Pipeline and the Common Astronomy Software Applications (CASA) package were adopted to reduce the visibility data of the VLA observations. The image analysis was carried out in MIRIAD. The resultant synthesized beam size was $\sim 1\farcs20 \times 0\farcs45$. The detection limit in a single spectral channel was $\sim$0.1 Jy beam^{-1} (5 times the noise level in these images). The positions and flux densities of the detected maser components (also called "maser spots" in this Letter) in each channel map were estimated by fitting a two-dimensional Gaussian brightness distribution using the MIRIAD task IMFIT. The typical uncertainty of the fitted position of maser components was smaller than $0\farcs01$. The absolute positional uncertainty of the VLA observations is less than $0\farcs02$, which mainly originates from the positional uncertainty of the calibrator. The full list of parameters measured from Gaussian fitting to each maser spot, for the four observed transitions, is available in Table 1.

2.3. Australia Telescope Compact Array (ATCA) Observations

ATCA observations of the 35.171 GHz 9_2–10_1 A^+ transition of $^{13}CH_3OH$ were conducted as part of a series of spectral line observations on 2019 March 7 (Breen et al. 2019). The ATCA was in the H214 array configuration, but as it was in scheduled maintenance, antennas 1 and 2 were not available. Observations were centered on the same position as the TMRT and VLA observations (see above), and the Compact Array Broadband Backend (CABB; Wilson et al. 2011) was configured in CFB 64M-32k mode. This mode provided a 64 MHz zoom band with 2048 channels, centered at the frequency of the 35.171 GHz $^{13}CH_3OH$ line (corresponding to a velocity coverage of 545 km s^{-1} and channel spacing of 0.27 km s^{-1}). This mode also allowed for two 2 GHz continuum bands to be observed simultaneously and these were centered at 35.3 and 38.4 GHz. Observations of G 358.93-0.03 were interspersed with observations of B1741−312 every 10 minutes for phase calibration, and observations of PKS B1253−055 and PKS B1934−638 were made for bandpass and primary flux density calibration. Pointing corrections were made on B1741−312 once per hour. Observations were conducted over $\sim$5.5 hr and resulted in 2.4 hr integration time on the science target.

Data were reduced using the MIRIAD software package. The broadband continuum data were used to fit a flux model to PKS B1253−055, which was then bootstrapped to PKS B1934−638 for absolute calibration. This was then used to determine the bandpass and amplitude scaling of the 64 MHz zoom band. The absolute position and the spectrum were extracted from the image cube. The primary flux density calibration is accurate to better than 10%. The synthesized beam size was $\sim 6\farcs0 \times 3\farcs0$. The detection limit in a single spectral channel was $\sim$0.1 Jy beam^{-1} ($5\sigma_{\rm rms}$). The position accuracy of the maser emission from the ATCA observations is better than $0\farcs2$.

[20] [1] M2O is a global co-operative of maser monitoring programs; see https://m2o.hartrao.ac.za/.

Table 1
Parameters Measured from the Gaussian Fitting to Maser Spots at the $^{13}CH_3OH$ and CH_3OH Transitions Detected from the VLA Observations

Transition	Velocity (km s^{-1})	Flux Density (Jy beam^{-1})	x (arcsec)	σ_x (arcsec)	y (arcsec)	σ_y (arcsec)	T_b (10^4 K)
(1)	(2)	(3)	(4)	(5)	(6)	(7)	(8)
14.300 GHz $^{13}CH_3OH$	−15.20	5.96	−0.069	0.002	−0.038	0.004	10.8
...	−15.28	26.67	−0.073	0.002	−0.055	0.003	48.8
...	−15.36	39.31	−0.076	0.002	−0.068	0.003	72.6
			...				
14.782 GHz $^{13}CH_3OH$	−15.08	0.16	−0.043	0.011	−0.030	0.021	0.3
...	−15.16	0.19	−0.082	0.008	−0.065	0.016	0.4
...	−17.53	5.96	−0.110	0.002	0.104	0.003	10.7
			...				
12.178 GHz CH_3OH	−14.72	0.57	−0.066	0.009	0.020	0.015	0.9
...	−14.82	1.77	−0.012	0.005	0.115	0.009	2.7
...	−17.22	709.35	0.085	0.004	0.138	0.007	1082.3
			...				
12.229 GHz CH_3OH	−14.97	3.94	0.000	0.004	0.034	0.008	6.1
...	−15.07	23.98	0.006	0.005	0.063	0.008	37.1
...	−15.16	180.99	−0.002	0.004	0.041	0.007	281.0
			...				

Note. Column (1): maser transition; Column (2): spot velocity; Column (3): peak flux density; Columns (4)–(7): the positions with uncertainties in R.A. and decl. relative to the position (α = 17:43:10.1015, δ = −29:51:45.6936; J2000) of continuum emission; Column (8): lower limit of brightness temperature of the maser spot.

(This table is available in its entirety in machine-readable form.)

3. Results and Discussions

3.1. Detections of $^{13}CH_3OH$ Masers

Figure 1 shows the spatial distribution and spectra of the maser emission from the 14.300 and 14.782 GHz $^{13}CH_3OH$ transitions obtained from the VLA observations. The 14.300 GHz transition exhibits strong emission with a peak intensity of ∼40 Jy beam^{-1} and multiple spectral components covering the velocity range −18 to −15 km s^{-1} in the LSR frame, while the 14.782 GHz transition has a lower peak flux density (∼6 Jy beam^{-1}) and three narrow spectral features. Interferometric imaging shows that the maser spots from the 14.300 GHz transition are distributed in a ring-like structure, whereas the 14.782 GHz transition is confined to three small clusters (see Figure 1). The emission from both the isotopic transitions is likely associated with a rotating molecular ring or disk (see the Appendix for details of the rotational model). The total spatial extent of the emission from the two transitions is ∼0.″3, and corresponds to a linear scale of ∼2000 au, for an assumed kinematic distance of 7.0 kpc (estimated using the kinematic Galactic rotation model reported in Reid et al. 2016 and a systemic source velocity of $V_{\rm LSR}$ = −16.5 km s^{-1}). The VLA observations allow us to place a lower limit of 2 × 10^3 K on the brightness temperature of the detected maser spots (see Table 1). These values are much higher than the maximum kinetic temperature (∼100–300 K) of typical thermal emission associated with hot molecular cores in HMYSOs, confirming that it is maser emission detected in these two transitions.

In addition to the 5_1–6_0 A^+ and 2_0–3_{-1} E transitions, emission from the 9_2–10_1 A^+ (35.171 GHz) transition of $^{13}CH_3OH$ was detected with the ATCA. This is the analog of the rare 23.1 GHz Class II transition of CH_3OH, which itself has been detected toward only a handful of sources (Cragg et al. 2004). The emission from the 9_2–10_1 A^+ line has a peak intensity of 3.4 Jy beam^{-1} at −15.3 km s^{-1} (see the top panel of Figure 2). Although the locations of the spots in the 9_2–10_1 A^+ line emission from the ATCA observations have a larger uncertainty (∼0.″2), they are consistent with those of the two $^{13}CH_3OH$ lines observed with the VLA (see the bottom panel of Figure 2). Based on the similar spectral profiles and spatial distributions, the detected $^{13}CH_3OH$ transitions can be divided into five groups, labeled as (a)–(e) (see Figure 2).

The isotopic methanol maser spots are distributed around a millimeter continuum source (see Figures 1 and 2) detected in Atacama Large Millimeter/submillimeter Array (ALMA) observations at a wavelength of 0.89 millimeters (Brogan et al. 2019). This continuum source appears to be the exciting source for the maser emission in this region, and the absence of centimeter continuum emission (to a 3σ detection limit of detection of 20 μJy) at this location in the VLA observations indicates that the exciting source is an HMYSO at a very early evolutionary stage.

3.2. Comparisons of the $^{13}CH_3OH$ and CH_3OH Masers

The 2_0–3_{-1} E and 16_5–17_4 E CH_3OH maser transitions (accurate rest frequencies of 12.178593 and 12.229348 GHz, respectively; Müller et al. 2001, 2005), were also detected during the same VLA observations. Their spectra and spatial distributions are presented in panels (c) and (d) of Figure 1. Figure 2 shows a comparison of the spectra and spatial distributions of the three $^{13}CH_3OH$ and two CH_3OH transitions detected in the VLA and ATCA observations. Both the 12.178 and 12.229 GHz CH_3OH transitions show brighter maser emission than any of the three isotopic methanol transitions, with peak flux densities of ∼600–700 Jy and spectral peaks at −17.3 and −15.5 km s^{-1}. The overall distribution of maser spots in these two CH_3OH maser lines shows the presence of an elongated structure with a velocity gradient (marked with the black curve in the bottom

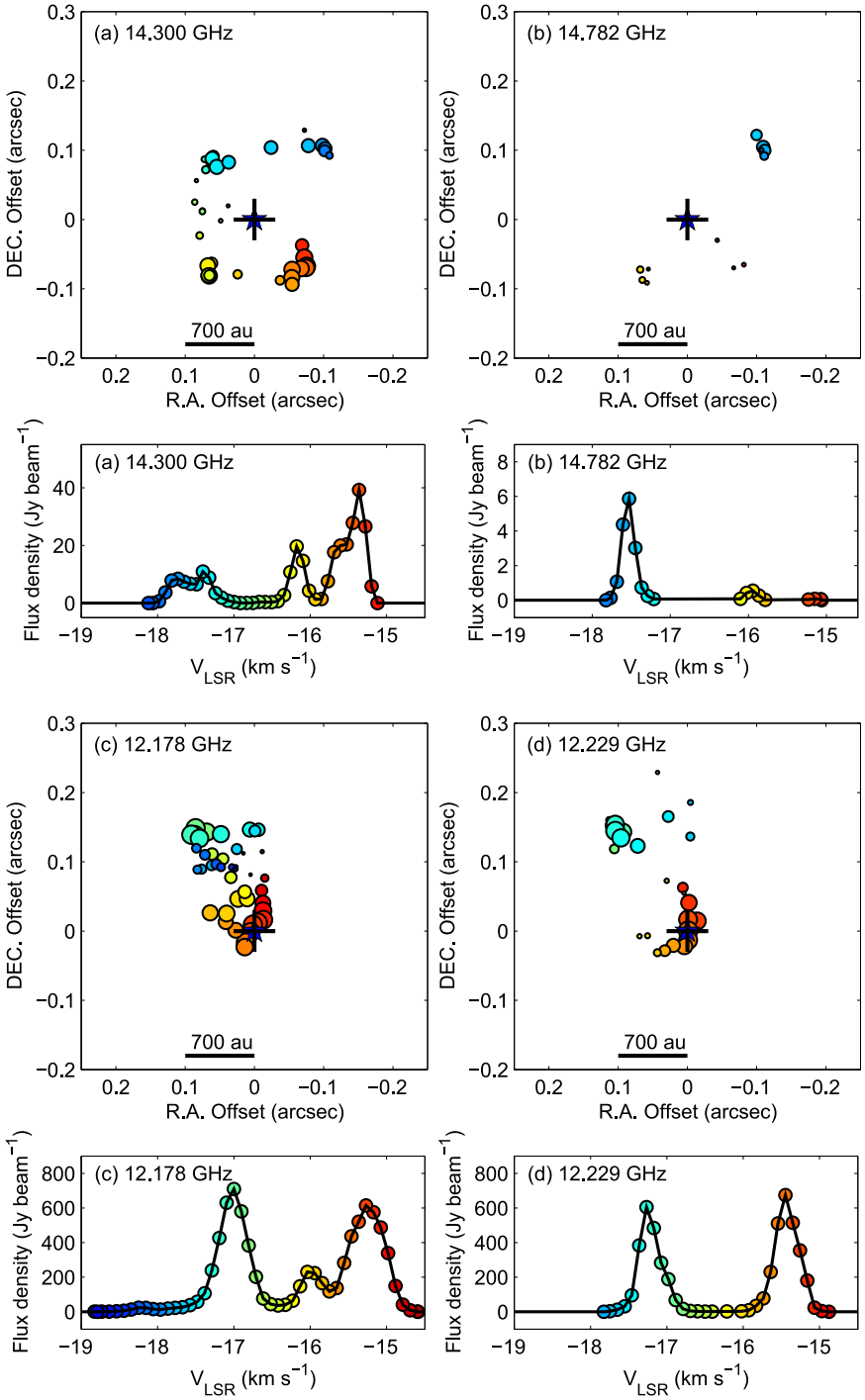

Figure 1. Spatial distribution (upper) and spectra (lower) of $^{13}CH_3OH$ and CH_3OH maser transitions detected toward G358.93-0.03 with the VLA. Panels (a)–(d) represent the 5_1–6_0 A^+ (14.300) GHz and 2_0–3_{-1} E (14.782 GHz) $^{13}CH_3OH$ transitions and the 2_0–3_{-1} E (12.178 GHz) and 16_5–17_4 E (12.229 GHz) CH_3OH transitions, respectively. Each maser spot is represented by a filled circle whose area is proportional to its flux density (multiplied by 0.05 for the CH_3OH transitions) on a logarithmic scale and whose color indicates its Doppler velocity with respect to the local standard of rest (LSR). The distribution of the maser emission is relative to the millimeter continuum source at $\alpha = 17{:}43{:}10.1015$, $\delta = -29{:}51{:}45.6936$ (J2000), detected in the line-free channels of ALMA observations (Brogan et al. 2019), and marked with a blue star. The black cross shows the absolute positional uncertainty ($\sim 0\farcs03$) of the millimeter continuum source. The relative positional uncertainty of each maser spot is typically less than $0\farcs01$, and hence is not shown in the plot. The absolute positional uncertainties of the VLA images are less than $0\farcs02$.

panel of Figure 2). It has been shown both observationally and theoretically that Class II methanol masers can be produced in the inner parts of accretion disks and outflows close to HMYSOs (Parfenov & Sobolev 2014; Sanna et al. 2015, 2017). Such elongated structures are often traced by methanol maser emission (Sanna et al. 2017) and likely reveal active gas flows around HMYSOs, although the direction of these flows (i.e., inflow or outflow; Bartkiewicz et al. 2009; Frank et al. 2014) are yet to be determined.

Comparison of the spatial and spectral distribution of the maser emission from the $^{13}CH_3OH$ and CH_3OH transitions shows that they have significant differences (Figure 2). The

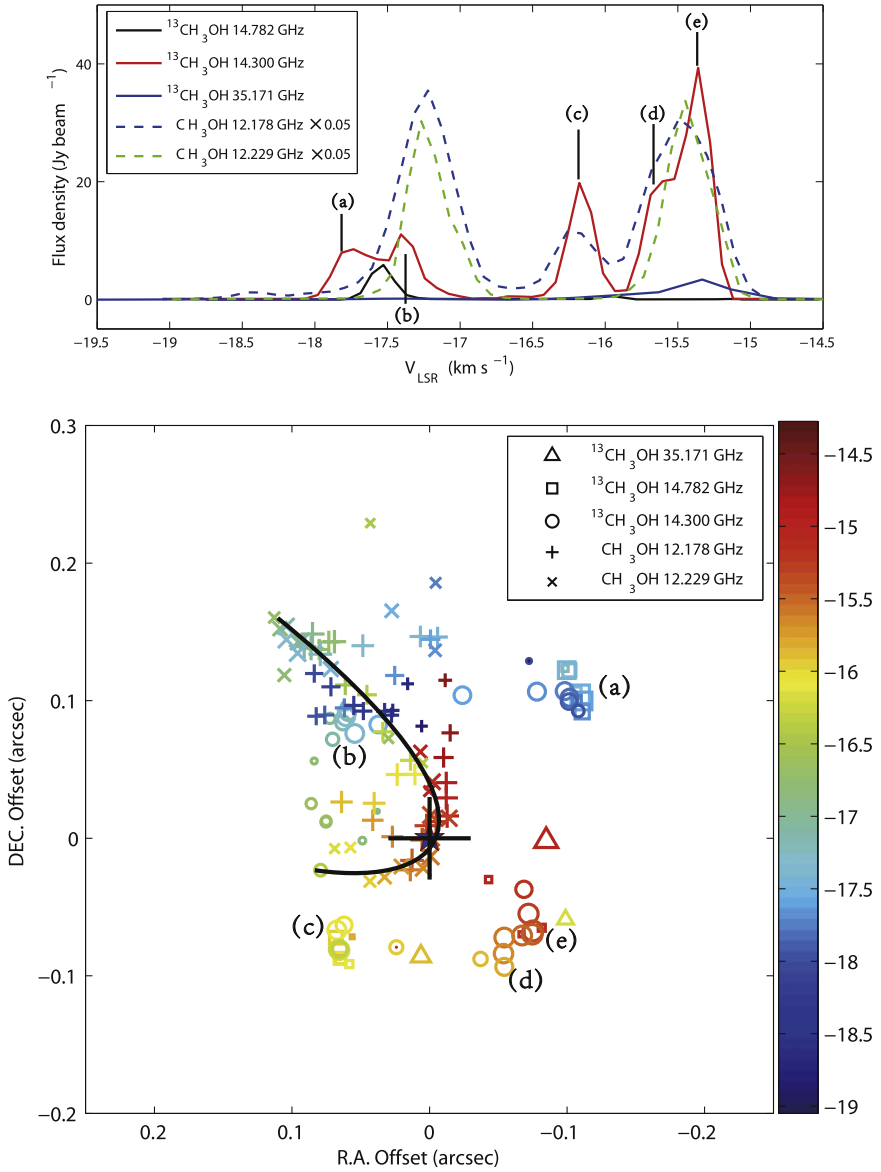

Figure 2. Comparison of the spectra and spatial distributions of the CH_3OH and $^{13}CH_3OH$ masers. The top panel shows the maser spectra from the 5_1–6_0 A^+ (14.300 GHz), 2_0–3_{-1} E (14.782 GHz) and 9_2–10_1 A^+ (35.171 GHz) $^{13}CH_3OH$ transitions and the 2_0–3_{-1} E (12.178 GHz) and 16_5–17_4 E (12.229 GHz) CH_3OH transitions. The bottom panel shows the spatial distributions of all five transitions. Note that the position uncertainty for the ATCA observation of the 9_2–10_1 A^+ (35.171 GHz) transition is $\sim 0\farcs2$ for the emission shown in the plot. Labels (a)–(e) indicate the five groups of the detected $^{13}CH_3OH$ transitions according to their similar spectral profiles and spatial distributions. The blue star and black cross are same as those shown in Figure 1. The black curve traces the overall distributions of the two CH_3OH masers, determined by visual inspection.

emission from the 14.300 GHz and 14.782 GHz $^{13}CH_3OH$ lines is predominantly located west and south of CH_3OH emission, and at these locations only isotopic methanol maser emission is observed. With the exception of a small proportion of 14.300 GHz $^{13}CH_3OH$ and 12.178 GHz CH_3OH maser spots around region (b), the areas showing methanol and isotopic methanol masers are disjointed.

Emission at 12.178 and 14.782 GHz is from the 2_0–3_{-1} E transition of CH_3OH and $^{13}CH_3OH$, respectively, and these represent the best opportunity for a direct comparison of the similarities and differences in the two methanol species. The intensity of the $^{13}CH_3OH$ maser is more than a factor of 100 weaker than from the CH_3OH transition at the same epoch and although the velocity ranges are similar, the three spectral features in the $^{13}CH_3OH$ all peak at different velocities from the three primary CH_3OH spectral components. Interestingly, the peak velocities of the blue and redshifted components from the $^{13}CH_3OH$ are slightly blueward and redward of the CH_3OH peaks at similar velocities (see Figure 2). Furthermore, when we compare the spatial emission from these two transitions we can see that they are entirely disjoint.

Predictions of Johns et al. (1998) suggest that because $^{13}CH_3OH$ has a molecular structure that is very similar to the methanol main species, the 2_0–3_{-1} E transition of CH_3OH and $^{13}CH_3OH$ should be excited under the same conditions, with intensity differences almost totally due to the abundance ratio of the two species that corresponds to the difference in their column densities. The absence of emission from the 14.782 GHz 2_0–3_{-1} E $^{13}CH_3OH$ transition (an assumed upper limit of flux density of 0.1 Jy; corresponding to $5\sigma_{rms}$ in the VLA observation), at the location of

the brightest the 12.178 GHz maser implies an intensity ratio $S_{12.178}$:$S_{14.782}$ in excess of 7000:1 for the −17.22 km s^{-1} spectral component (see Table 1). Conversely, for the location of the brightest 14.782 GHz 2_0–3_{-1} E $^{13}CH_3OH$ maser at a velocity of −17.53 km s^{-1} we have $S_{12.178}$:$S_{14.782}$ less than 0.017:1 (see Table 1), whereas the intuitive expectation is that there should be strong 12.178 GHz emission from this location (Johns et al. 1998). However, Sobolev & Deguchi (1994) have shown that the saturation effects strongly influence distribution of the methanol-level population numbers under conditions of Class II methanol maser excitation, and the saturation effects can be greatly different from those in the two-level case. This is strongly supported by calculations of Cragg et al. (2005), which predict that the brightness of the strongest methanol masers can experience a fast drop when the column density exceeds a certain threshold value. The limited modeling that has been undertaken of Class II $^{13}CH_3OH$ masers and saturated CH_3OH masers to date cannot provide a clear explanation for the observational data in G358.93-0.03. Hence, additional modeling of the isotopic masers is now a topic for serious attention, but undertaking such investigations is beyond the scope of the current work.

Johns et al. (1998) also predicted the cases for the 5_1–6_0 A^+ transitions of CH_3OH and $^{13}CH_3OH$; however, we do not have data for the 6.668 GHz CH_3OH transition at the same epoch and because of the very rapid evolution of the intensity and spatial distributions observed in this transition (Burns et al. 2020), we cannot make a meaningful comparison.

3.3. A Rapid Decay of the $^{13}CH_3OH$ Maser Lines

Monitoring of the 14.300 and 14.782 GHz $^{13}CH_3OH$ lines with the TMRT over the period 2019 April 2–15 shows a significant decline in the maser emission for all the detected spectral features (Figure 3). The decline appears to be approximately exponential, but the maser features at different velocities show different decay curves (see the middle panel of Figure 3). If we assume that each of the components has a similar decay half-life, this suggests that these maser components, which are usually located in slightly different spatial regions (see Figure 2), are at different phases of decay. The physical basis for the timescale and relative delays in the decay of the maser features is expected to be related to variability in the physical conditions or geometry of the masing region. A decline in gas density or temperature (or both) will lead to a gradual fading of the maser emission. Unfortunately, we do not have any observations prior to the peak in the maser intensity for these transition lines. We find that by introducing delays (4.5, 9, 8, 2.5, and 2 day delays for the 14.300 GHz features (a)–(e) with regard to the 14.782 GHz feature (a), respectively), it is possible to produce normalized decay curves that agree closely (see the bottom panel of Figure 3). This suggests that the decay half-period for all the maser components is approximately 10 days.

The speed of the decay prevents the populations of the methanol levels from reaching statistical equilibrium because the pumping cycles of methanol masers are long and numerous and it takes up to hundreds of days for their realization (Sobolev & Deguchi 1994). It is therefore likely that we are dealing with masers operating under rapidly changing conditions. Fast variability, which is correlated for rather distant positions (i.e., 1300 au between components (b) and (e)), suggests that in our case changes in the excitation conditions propagate with very high speed (approximately at the velocity

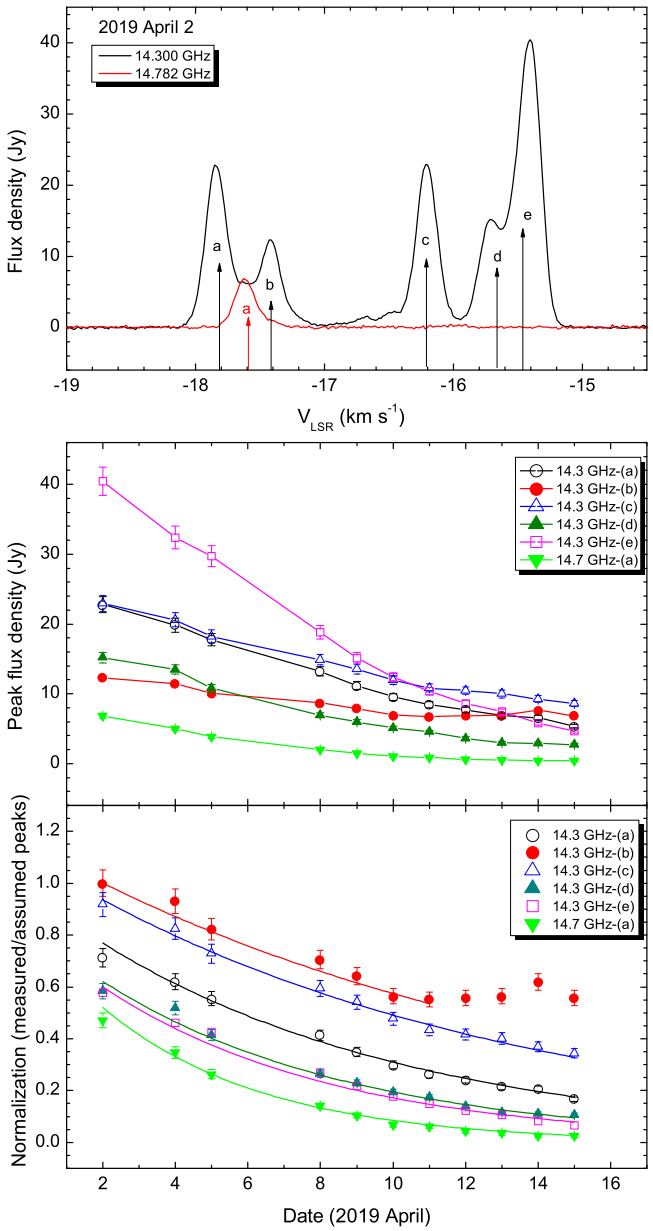

Figure 3. Decay of the peak flux density of maser features in the 14.300 and 14.782 GHz $^{13}CH_3OH$ lines obtained from monitoring observations with TMRT over the period 2019 April 2–15. The top panel gives an example spectra observed on 2019 April 2, with corresponding spectral features are labeled (a)–(e). The middle panel shows the variability of these maser components during the monitoring observation dates. The bottom panel is the normalized decay that is obtained from the ratio of the measured peak to the assumed maximum peak for each maser feature under the assumption that the half-life period of the decay of all the maser features is the same (10 days).

of light with a delay of 8 days between (b) and (e)) and cannot be associated with transfer of material. Therefore, variability is produced by the changes in the radiation field and confirms a radiative origin of the isotopic maser pumping.

3.4. $^{13}CH_3OH$ Masers Associated with an Accretion Burst

Class II methanol masers are pumped by infrared radiation, located in highly dynamic regions, and amplify background emission. The occurrence of methanol maser flares in many transitions simultaneously is best described for the case of

periodically variable sources. The same reasoning can be applied for common flares because the basics of the maser pumping are the same and imply changes in the pumping conditions. So, methanol maser flares can be associated with the increase of the radiation field, possibly due to accretion outbursts (Garatti et al. 2017) or the protostellar luminosity bursts (Inayoshi et al. 2013). A direct link between the 6.7 GHz Class II CH_3OH maser flaring and accretion bursts has recently been established for a number of high-mass star formation regions (Hunter et al. 2017, 2018; Moscadelli et al. 2017). The accretion burst process is possibly caused by disk fragmentation and can be periodic (Meyer et al. 2019) or stochastic (Garatti et al. 2017). An accretion burst will occur when a dense clump rapidly accretes onto the protostar, causing the luminosity to increase. For G358.93-0.03 (sub) millimeter observations of the continuum emission have not detected changes (Brogan et al. 2019), but the FIR emission has shown a significant increase in luminosity (Burns et al. 2020; B. Stecklum et al. 2020, in preparation) which supports an accretion burst having occurred in this source.

The Tianma monitoring of the isotopic masers suggests that the radiation from G358.93-0.03 declined over the period 2019 April 2–15, perhaps indicating the end of the flaring event. If the unusual maser conditions were produced by an accretion burst in G358.93-0.03, it is expected to be very short (a timescale of a few months is derived from the M2O maser monitoring project); however, the process could repeat when another dense clump accretes onto the HMYSO. New detections and monitoring observations of isotopic methanol maser transitions are necessary to clarify whether the accretion burst repeats (and if so on what timescale), or if it is a transient stochastic phenomenon during the formation of high-mass stars.

4. Summary

Using single-dish (TMRT) and interferometric (VLA and ATCA) observations, we made the first detections of the isotopic methanol masers at three transitions (14.300, 14.782, and 35.171 GHz) in an HMYSO (G358.93-0.03). This source may be associated with an accretion burst event due to the fact that it shows a flare in the 6.7 GHz methanol maser emission since 2019 January with an increase in FIR emission at the time of the maser flare. Therefore, this source may be able to provide unique high spatial and temporal resolution information on accretion burst process through the impact of the changing radiation field on methanol maser pumping. The totally different spectral and spatial distribution between the $^{13}CH_3OH$ and CH_3OH masers obtained at the same epoch reveals that isotopic methanol masers are bright under different physical conditions compared to main methanol masers. New pumping modeling of the isotopic masers is required to explain the observed differences between them. A rapid decay (a timescale of only $\sim$ one month) of the isotopic methanol masers detected from the monitoring observations is likely associated with rapid changes in the radiation filed due to the putative accretion burst event of this source. Therefore, the isotopic methanol masers may be an effective probe for the accretion burst process during the formation of the most massive stars.

We thank an anonymous referee for helpful comments that improved the manuscript. We thank TMRT, ATCA, and VLA staff for assistance obtaining the data presented in this Letter. The National Radio Astronomy Observatory is a facility of the National Science Foundation operated under agreement by the Associated Universities, Inc. The ATCA is part of the Australia Telescope National Facility. X.C. was supported by the National Natural Science Foundation of China (11590781, 11873002, 11590780, 11590784) Project Supported by Guangdong Province Universities and Colleges Pearl River Scholar Funded Scheme (2019), and the major scientific research project of Guangdong regular institutions of higher learning (2017KZDXM062). A.M.S. was supported by the Russian Science Foundation (grant 18-12-00193). S.P.E. acknowledges the support of ARC Discovery Project (project No. DP180101061).

Appendix
A Rotational Disk or Ring Model for the $^{13}CH_3OH$ Masers

The distribution of the $^{13}CH_3OH$ masers suggests that they may be associated with a rotating structure, such as a ring or disk around the central star. To test this, if we assume that the gravitational field is dominated by the central star and the $^{13}CH_3OH$ masers have circular rotations, one can model their spatial and velocity distributions based on Keplerian rotation. In this case, the radial velocity can be expressed as

$$V_{\rm lsr}(x, y) = \sqrt{\frac{GM_*}{R}}\cos\phi\sin i \quad (1)$$

where i is the inclination angle between the orbital plane and the sky plane, and variable ϕ is the azimuthal angle in the orbital plane with the origin ($\phi = 0$) set to be along the crossing line between orbit plane and the sky plane, as shown in Figure 4. The coordinates (x, y) are the position on the sky plane, which are converted from the angles i and ϕ, using $x = R\sin\phi\cos i$ and $y = R\cos\phi$. The position (x, y) can be also transformed into the R.A.–decl. frame.

The radial velocity field of the best-fit rotating plane is shown in color scale in Figure 4. The best-fit model places the $^{13}CH_3OH$ masers at a bulk radius of $R_0 = 0\farcs11 \pm 0.03$ with $i = 40^\circ \pm 5$, and the stellar mass is constrained to be $M_* = (5 \pm 1)M_\odot$. The radial velocities of the $^{13}CH_3OH$ masers are a reasonable fit to the modeled Keplerian rotation at R_0 projected onto the sky plane. There are only seven maser points located at larger distances. As the region may have complicated gas motions, there would be no conflict if some $^{13}CH_3OH$ masers are not associated with the rotating structure. The velocity distribution of the orbit is also in reasonable agreement with the previously measured velocity gradient from the natal CH_3CN core (Brogan et al. 2019), suggesting that the $^{13}CH_3OH$ masers may trace a ring or disk in the inner part of the entire rotating core.

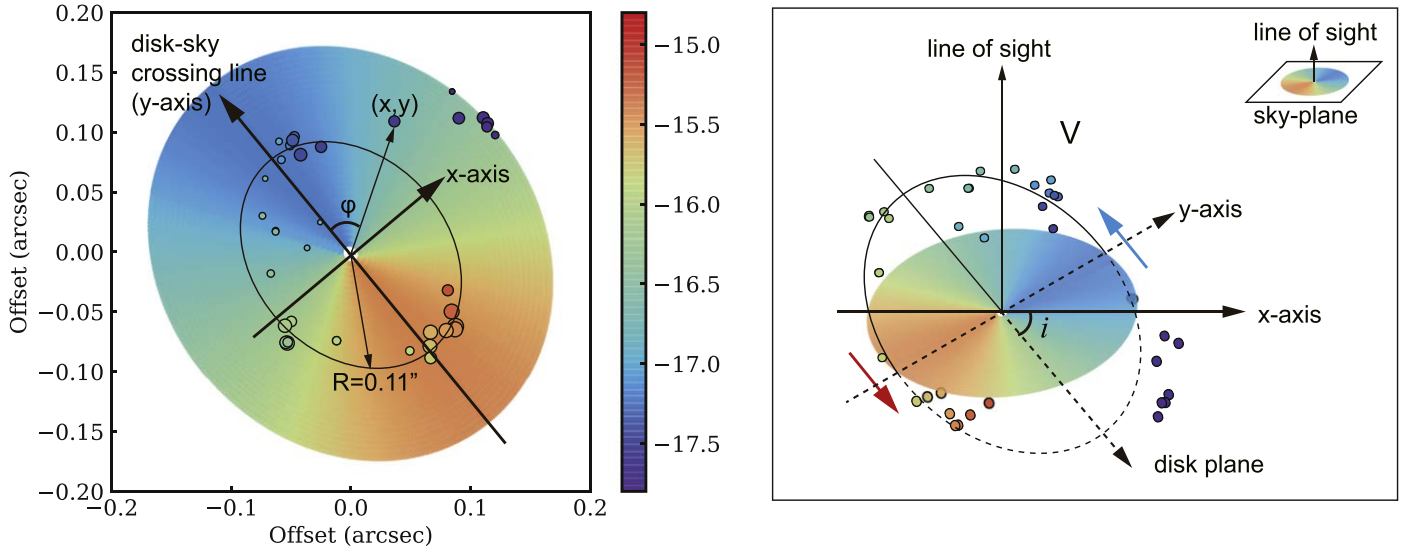

Figure 4. Left panel: the best-fit radial velocity field projected onto the sky plane as modeled from Equation (1), with the 14.300 GHz $^{13}CH_3OH$ maser spots overlapped. Right panel: a schematic view showing the spatial layout of the modeled rotation frame.

ORCID iDs

Shari L. Breen https://orcid.org/0000-0002-4047-0002
Simon P. Ellingsen https://orcid.org/0000-0002-1363-5457
Todd R. Hunter https://orcid.org/0000-0001-6492-0090
Crystal Brogan https://orcid.org/0000-0002-6558-7653
Koichiro Sugiyama https://orcid.org/0000-0002-6033-5000
Ross A. Burns https://orcid.org/0000-0003-3302-1935
Karl Menten https://orcid.org/0000-0001-6459-0669
Tomoya Hirota https://orcid.org/0000-0003-1659-095X
Kee-Tae Kim https://orcid.org/0000-0003-2412-7092
James Chibueze https://orcid.org/0000-0002-9875-7436

References

Bartkiewicz, A., Szymczak, M., van Langevelde, H. J., Richards, A. M. S., & Pihlström, Y. M. 2009, A&A, 502, 155
Breen, S. L., Sobolev, A. M., Kaczmarek, J. F., et al. 2019, ApJL, 876, L25
Brogan, C. L., Hunter, T. R., Towner, A. P. M., et al. 2019, ApJL, 881, L39
Burns, R. A., Sugiyama, K., Hirota, T., et al. 2020, NatAs, in press
Chen, X., Gan, C.-G., Ellingsen, S. P., et al. 2013, ApJS, 206, 9
Cragg, D. M., Sobolev, A. M., Caswell, J. L., Ellingsen, S. P., & Godfrey, P. D. 2004, MNRAS, 351, 1327
Cragg, D. M., Sobolev, A. M., & Godfrey, P. D. 2005, MNRAS, 360, 533
Ellingsen, S. P., Voronkov, M. A., Cragg, D. M., et al. 2007, in IAU Symp. 242, Astrophysical Masers and their Environments, ed. J. M. Chapman & W. A. Baan (Cambridge: Cambridge Univ. Press), 213
Frank, A., Ray, T. P., Cabrit, S., et al. 2014, in Protostars and Planets VI, ed. H. Beuther et al. (Tucson, AZ: Univ. Arizona Press), 451
Garatti, A. C. o., Stecklum, B., Lopez, R. G., et al. 2017, NatPh, 13, 276
Hunter, T. R., Brogan, C. L., MacLeod, G., et al. 2017, ApJL, 837, L29
Hunter, T. R., Brogan, C. L., MacLeod, G. C., et al. 2018, ApJ, 854, 170
Inayoshi, K., Sugiyama, K., Hosokawa, T., et al. 2013, ApJL, 769, L20
Johns, K. P., Cragg, D. M., Godfrey, P. D., & Sobolev, A. M. 1998, MNRAS, 300, 999
Kuiper, T. B. H., Peters, W. L., III, Gardner, F. F., Whiteoak, J. B., & Reynolds, J. E. 1989, ApJL, 340, L41
Leurini, S., Menten, K. M., & Walmsley, C. M. 2016, A&A, 592, 31
MacLeod, G. C., Sugiyama, K., Hunter, T. R., et al. 2019, MNRAS, 489, 3981
Menten, K. M. 1991, ApJL, 380, L75
Menten, K. M., & Batrla, W. 1989, ApJ, 341, 839
Meyer, D. M.-A., Vorobyov, E. I., Elbakyan, V. G., et al. 2019, MNRAS, 482, 5459
Minier, V., Ellingsen, S. P., Norris, R. P., & Booth, R. S. 2003, A&A, 403, 1095
Moscadelli, L., Sanna, A., Goddi, C., et al. 2017, A&A, 600, L8
Müller, H. S. P., Menten, K. M., & Mäder, H. 2004, A&A, 428, 1019
Müller, H. S. P., Schlöder, F., Stutzki, J., & Winnewisser, G. 2005, J. Mol. Struct., 742, 215
Müller, H. S. P., Thorwirth, S., Roth, D. A., & Winnewisser, G. 2001, A&A, 370, L49
Parfenov, S. Yu., & Sobolev, A. M. 2014, MNRAS, 444, 620
Reid, M. J., Dame, T. M., Menten, K. M., & Brunthaler, A. 2016, ApJ, 823, 77
Sanna, A., Moscadelli, L., Surcis, G., et al. 2017, A&A, 603, 94
Sanna, A., Surcis, G., Moscadelli, L., et al. 2015, A&A, 583, L3
Sobolev, A. M., & Deguchi, S. 1994, ApJ, 433, 719
Sugiyama, K., Saito, Y., Yonekura, Y., & Momose, M. 2019, ATel, 12446, 1
Voronkov, M. A., Caswell, J. L., Ellingsen, S. P., Green, J. A., & Breen, S. L. 2014, MNRAS, 439, 2584
Wilson, W. E., Ferris, R. H., Axtens, P., et al. 2011, MNRAS, 416, 832
Xu, L.-H., Lees, R. M., Hao, Y., et al. 2014, JMoSp, 303, 1
Xu, Y., Li, J. J., Hachisuka, K., et al. 2008, A&A, 485, 729